

Computational Assessment of Afterburning Cessation Mechanisms in Fuel Rich Rocket Exhaust Plumes

William H. Calhoon, Jr.*

SPARTA, Inc.

December 4, 1998

20010126 050

ABSTRACT

A computational study was conducted to identify fundamental physical processes governing the cessation or shutdown of the afterburning of fuel rich rocket exhaust with the atmosphere. Several mechanisms were examined which are: 1) a relaminarization phenomenon, 2) a Damköhler number effect and 3) a classical flame extinction mechanism. Analysis of the simulation results revealed the relaminarization mechanism to be implausible while the Damköhler number effect and the flame extinction mechanisms were found to be valid. The extinction mechanism was also found to dramatically alter the emission characteristics and enhance the shutdown behavior which has important implications with respect to radiative heat transfer to the body and missile defense systems. This is a significant finding because strain rate induced extinction is a previously unrecognized phenomena occurring in rocket

Staff Scientist, Member AIAA
AFRL/PRSA
10 East Saturn Blvd.
Edwards AFB, CA 93524-7680
email:calhoon@mohawk.ple.af.mil

exhaust plumes during afterburning cessation.

1 Introduction

Future development of booster systems will be substantially influenced by the temperature environment which is encountered in the body's base region. Heat transfer to the body results from both convective and radiative phenomena. For fuel rich systems exhibiting strong afterburning of the engine exhaust species with the atmosphere, the radiative component of the base heat transfer rate may be the dominant feature.¹ As altitude or time after launch is increased, the radiative heat transfer rate will eventually show a large drop in magnitude,² associated with the shutdown of afterburning in the plume. Shutdown here does not refer to the termination of the booster engine but to the shutdown or cessation of afterburning of the engine exhaust with the atmosphere, occurring with continuous engine operation. The time (or altitude) and rate of decay of the afterburning shutdown event will determine the total heat transfer to the body and thus the design criteria for the components in the base region. The radiative emissions during the shutdown event are also relevant to missile defense systems. Consequently, an accurate characterization of afterburning shutdown or cessation events is required.

Accurately characterizing exhaust plume afterburning and afterburning cessation is a difficult problem due to the complexities of the physical phenomena occurring in these flows. For example, strong turbulence-chemistry interactions may exist in the high speed plume shear layer between the exhaust and external flow. These interactions not only affect species production and temperature distributions but may also impact the radiation predictions.³

In addition, a complex shock wave pattern⁴ exists in the plume to equilibrate the exhaust flow pressure with the atmosphere. Reflected shocks may excite vortical roll up of the shear layer (e.g., Ref. 5) enhancing mixing and may also provide a temperature rise to stabilize afterburning. These difficulties are also exacerbated by 3-D effects in multiple nozzle systems.

Additional complications arise in exhaust plume analysis due to uncertainties with regard to the combustion and mixing processes occurring within the engine itself. First, the injector pattern and any acoustic baffles within the engine set up fuel-oxidizer striations which may not be completely homogenized before exiting into the plume due to incomplete mixing. Second, fuel film cooling and regenerative cooling of the fuel and oxidizer may have a significant impact on the species concentration and temperature distributions. Third, the spectral distribution of the turbulent kinetic energy within the engine nozzle has also been shown to strongly affect afterburning and shutdown characteristics.⁶ Fourth, the presence of particulates may have a significant impact on the plume thermal structure and flowfield^{7,8} which in turn will affect afterburning and shutdown. Deficiencies in characterizing these uncertainties will inhibit accurate predictions of plume afterburning and shutdown, resulting in poor predictions of radiative emissions and heat transfer to the body.

The character of the afterburning shutdown events has been observed to vary among different propulsion systems. For example, during shutdown some systems exhibit a gradual drop in total radiant intensity over a wide altitude range while other systems shutdown very rapidly over a much narrower range. Application of the engineering level modeling techniques to predict afterburning cessation has been relatively successful for systems which exhibit the gradual drop off type of shutdown event. However, for systems showing abrupt shutdown, engineering models have been less successful. To improve the accuracy of the engineering

codes, a basic understanding of the physical mechanisms producing afterburning cessation must be gained. Such an understanding is a prerequisite for future development efforts to capture the essential physics without unnecessarily compromising computational efficiency.

No previous study has been undertaken to specifically investigate afterburning shutdown in fuel rich exhaust plumes with altitude increase. However, afterburning shutdown mechanisms have been informally proposed which include 1) a relaminarization/mixing transition phenomenon and 2) a Damköhler number¹ effect. It is also proposed here that a classical flame blow-off/extinction mechanism may be responsible for afterburning shutdown. The relaminarization mechanism is based on the assertion that the shear layer Reynolds number (Re) reduction with increasing altitude will cause the mixing transition⁹ to be reached so that afterburning may not be sustainable due to a reduced molecular mixing rate. A Damköhler number effect producing afterburning cessation results from the competition between turbulent mixing and chemical heat release and radical production. Turbulent mixing continually cools the hot engine exhaust through mixing with the atmosphere while combustion processes release heat and produce radical species required to ignite the flow. Afterburning will not be sustainable when turbulent mixing can cool the plume at a higher rate than chemical processes can produce heat and a radical pool sufficient to initiate burning. For the classical flame extinction mechanism, decreasing reaction rates with increasing altitude may cause the plume shear layer flame to become locally extinguished due to high turbulent mixing (or strain) at the small spatial scales. This will result in a delay in the onset of afterburning to a significant distance downstream of the engine nozzle exit plane. This delay distance will increase with altitude until the shear layer flame eventually blows-off (i.e., afterburning

¹The Damköhler number is the ratio of the plume characteristic mixing and chemical time scales and will be defined in a later section.

shutdown).

The purpose of this study was to computationally evaluate the plausibility of the aforementioned mechanisms to produce afterburning cessation in fuel rich exhaust plumes. This is a first of its kind investigation and was accomplished through a parametric study of the afterburning characteristics of a generic amine booster. This study considered only a single nozzle configuration to assess these mechanisms before a more complex 3-D configuration is studied. To reduce the parameter space of the study, it was assumed that no particulates were present in the flow and that the previously mentioned "real" engine effects (e.g., mixing inefficiency, regenerative cooling, etc.) were negligible.

The organization of this paper is as follows. The next section discusses the computation methodology used to carry out the simulations of the parametric study. Section 3 describes the application of this methodology to the rocket plume simulations considered here. Section 4 outlines the parametric study and presents results. Section 5 presents conclusions drawn from this study.

2 Computational Methodology

Turbulence near the rocket body and in the plume causes the flowfield to be highly unsteady and contain a wide range of turbulence length scales due to the high Reynold numbers typically encountered in this type of flow. To accurately capture this unsteady behavior, an unsteady simulation methodology such as large-eddy simulation (LES) is required. However, simulating the entirety of the rocket body, base region and plume, as considered here, precludes use of unsteady simulation approaches such as LES due to grid resolution require-

ments and CPU availability. Consequently, a steady state, Reynolds averaged approach has been adopted for this study.

The body and plume flowfields were analyzed using the structured, compressible Navier-Stokes (NS) flow solver "The General Aerodynamic Simulation Program" (GASP).¹⁰ This code solves the time averaged NS equations, including turbulence modeling, and is sufficiently general to accommodate chemically reacting flows and complex physical geometries. The code includes standard models for thermodynamic properties and detailed models for molecular transport properties. However, the present simulations only assumed constant Schmidt and Lewis numbers since molecular transport is not resolved in turbulent simulations using the Reynolds average approach. GASP achieves good computational efficiency through use of a fully parallelized shared memory implementation of the flow solver and also through the use of a parabolized form of the Navier-Stokes equations (PNS) for parabolic regions of the flow.

One major drawback of the GASP code is the lack of any treatment of the effect of turbulent fluctuations on the mean reaction rate in the species conservation equations. The mean reaction rate is calculated based on the mean temperature and species and neglects all turbulent fluctuations. Properly accounting for turbulence-chemistry interactions in combustion problems has been the subject of intense research for at least the last two decades. It is well known that neglecting turbulent fluctuations in the mean reaction rate terms can have significant consequences on the accuracy of a simulation. This deficiency precludes the use of GASP to evaluate the previously mentioned flame extinction mechanism in afterburning plumes. However, this extinction mechanism was evaluated using a separate code to be described in a later section.

Radiation calculations were decoupled from the flowfield simulations and were carried out as described by Ludwig and Malkmus¹¹ and Nelson.¹² Within this approach, radiation transport equations were solved using a band model for the gas phase absorption/emission, details of which are omitted here for brevity. The calculations for the present study used a wide band pass to encompass emissions from OH , CO , CO_2 and H_2O . Total radiation intensity predictions were also made using a field of view large enough to encompass the entire plume.

3 Rocket-Plume Simulations

The simulations considered in this study were carried out for a generic amine booster. Figure 1 presents a schematic of the axisymmetric geometric configuration. The exhaust nozzle was assumed to have an area ratio of 10 and protrude aft of the booster base as seen in Figure 1. The entire body-base-plume was simulated using GASP's NS and PNS solvers. The elliptic regions at the booster nose and in the base region were computed using the NS solver while the flow over most of the body and in the plume was treated using the PNS option. Each axisymmetric solution used $\sim 25,000$ grid points to resolve the body-base region and $\sim 60,000 - 75,000$ points for the plume, depending on the plume extent. The grids for each altitude were manually adapted around regions of high gradients to ensure proper resolution of the flow features. Adequacy of the grid resolution will be demonstrated in a later section.

The inflow boundary conditions at the nozzle exit plane were specified from a separate nozzle flow calculation. This solution was carried out using GASP's PNS solver with Chien's¹³ $k - \varepsilon$ turbulence model. The inflow boundary condition for this simulation was specified

from Mach line conditions at the throat generated using the TDK package.¹⁴ A standard nine species-ten reaction step mechanism for H_2/CO oxidation was used for this calculation as well as in the plume. Figures 2-4 present the radial variation of the major species, velocity and temperature, respectively, at the nozzle exit plane. For this case the flow is fairly uniform across the exit. The temperature (Figure 4) is $\sim 1330\text{ K}$ in the core with a much higher value at the nozzle wall due to adiabatic boundary conditions imposed there. The fuel rich conditions of the engine are evident in Figure 2 where there is an excess of CO and some H_2 with O_2 virtually depleted. This nozzle solution was assumed to be invariant with respect to altitude and was used for all the body-base-plume calculations.

The body-base-plume simulations were carried out by specifying the inputs to the GASP code as follows. The convective flux terms were discretized using the Van Leer flux split scheme with 3rd order MUSCL extrapolation and min-mod and/or ENO limiting. The viscous terms within GASP are discretized to second order accuracy. Turbulence was modeled using GASP's implementation of the compressibility corrected $k - \epsilon$ model. Flow along the body was assumed to be turbulent and a wall function was used. The turbulent Schmidt and Prandtl numbers were specified as 0.7 and 0.9, respectively.

Thermodynamic properties for the simulations were specified from standard polynomial fits except at the highest altitude which required the use of an equilibrium statistical mechanics approach due to the low temperature in the plume expansion region. Also, molecular transport properties were specified using Sutherland curve fits of viscosity and thermal conductivity for each species and the species diffusion coefficients were specified assuming a constant Schmidt number of 0.7.

4 Results and Discussion

In order to assess the physical mechanisms discussed in Section 1 which may be responsible for afterburning shutdown in fuel rich rocket plumes, a parametric study was conducted. This study considered parameters such as turbulence level and chemistry effects. The different cases considered in the study are listed in Table 1. The calculations were carried out using GASP's implementation of the $k - \varepsilon$ turbulence model and the previously mentioned 9 species-10 reaction CO/H_2 oxidation mechanism. The turbulent mixing for Case D was enhanced by increasing the production coefficient for the turbulent kinetic energy in the $k - \varepsilon$ model by 25%.

Experimentation was used to determine the altitude range over which afterburning shutdown occurred for this generic booster system, given an assumed trajectory profile. Within this range, simulations were conducted at altitudes of 25, 30 and 35 *km* for each case listed in Table 1. The Reynolds and Mach numbers based on freestream conditions and the body radius were $Re_\infty = 4 \times 10^6$, 2×10^6 and 1×10^6 and $M_\infty = 2.6$, 3.2 and 3.9 for the altitudes of 25, 30 and 35 *km*, respectively.

Figures 5 and 6 present contour plots of the temperature and CO_2 mole fraction, respectively, for Case A at 25 *km*. The features evident in this solution are typical for all cases. A curved "barrel" shock is evident in Figure 5(b) and is characteristic of highly underexpanded plume flows.⁴ This shock reflects off the axis of symmetry and interacts with the surrounding shear layer between the exhaust gases and the external flow. As seen in Figure 5(b), the reflected barrel shock serves to thicken the shear layer and enhance turbulent mixing as well as increase the shear layer temperature. This shock-shear layer interaction enhances burning

and acts as an anchor for the plume flame. This may be seen in Figure 6 which shows a rapid rise in CO_2 production at this point. This behavior is consistent with the work of Norris and Edwards⁵ who applied a much more general unsteady LES technique to simulate high speed reacting exhaust flows. Further downstream the plume is seen to be vigorously afterburning as apparent from the spatial distribution of CO_2 in Figure 6. These figures also show that in the farfield the plume flow closely resembles what is expected for a standard turbulent jet flame.

With increasing altitude, the point where CO_2 production begins to rise gradually moves further downstream for all cases. This is illustrated in Figure 7 which is a radial plot of CO_2 mole fraction for Case A at a fixed streamwise location x/x_{refl} in the plume for each altitude. The length scale x_{refl} is the distance between the nozzle exit plane and the barrel shock reflection point at the axis of symmetry. This reference length was found to approximately scale the results with respect to altitude so that a fixed value of x/x_{refl} corresponds to the same relative location in the plume for each case. As seen in Figure 7, the peak CO_2 value in the shear layer at 25 km is significantly higher than in the core ($y = 0$), indicating vigorous afterburning. With increasing altitude, ignition is delayed, resulting in lower peak CO_2 at 30 km. At 35 km the plume at this location is extinguished. Comparison of Case A and B results show that at 35 km the plume is mostly extinguished but is still burning to a small extent in the farfield.

The drop off of CO_2 production with respect to altitude for the various cases correspondingly results in a drop off of the radiation emission as can be seen in Figure 8. This figure presents contour plots of the spatial variation of the radiant intensity for Cases A, C and D. The left edge of each image in this figure corresponds to the nozzle exit plane and the

downstream direction is to the right. The spatial extent shown in Figure 8 encompasses the entire region of significant radiation for all cases except Case *C*. For this case, the lack of turbulent mixing causes the plume to be extraordinarily long and extend outside of the plotted domain shown in Figure 8. Species and temperature plots for Case *C* (not shown) reveal that this case produces vigorous afterburning for each altitude. However, the point at which product formation begins to rise rapidly moves further downstream with altitude increase, as evident in Figure 8. The other cases, however, are nearly extinguished at 35 km.

The apparent drop in spatial radiance seen in Figure 8 can be quantified in terms of the total radiant intensity which is the integration the spatial field over the entire field of view for each case. The total intensity is plotted in Figure 9 with all values being normalized by the result of Case *A* at 25 km. From this figure, Case *A* total intensity is seen to drop an order of magnitude over this altitude range and is close to the nonreacting value of Case *B* by 35 km. The emissions of Case *B* result mainly from the hot core flow downstream of the barrel shock reflection point and from high temperatures in the high speed shear layer resulting from viscous energy dissipation.

Similar to the results for Case *A*, Case *D* with enhanced turbulent mixing also exhibits an order of magnitude drop in total intensity over the altitude range considered. However, the Case *D* results are significantly lower for each altitude compared with Case *A*. This variation of radiation emissions with respect to turbulent mixing rate has been recognized by Dash *et al.*⁴ in the context of turbulence model assessment for plume flows. The increased mixing rate in Case *D* also increases the drop-off rate of the total intensity over Case *A*. This indicates an interaction between the turbulent mixing rate and the chemistry, since a simple axial scale reduction of the plume extent due to an increased turbulent mixing rate

alone would only produce a scale factor reduction in total intensity in Figure 9.

For Case *C*, the lack of turbulent mixing at all the simulated altitudes yields a thin shear layer with high temperatures due to viscous energy dissipation. Also, the centerline temperature downstream of the shock system levels out at approximately 900, 850 and 750 *K* for 25, 30 and 35 *km* altitudes, respectively. Consequently, both the hot core gases and the high temperature shear layer provide an ignition source for the plume, resulting in the vigorous afterburning and the high total intensities observed in Figure 9 for this case. These ignition sources will be present in the plume until much higher altitudes are reached (required to cool the core gases) and the shear is reduced across the layer (i.e., velocity matching of the core and external flow along the flight trajectory). Consequently, a purely laminar plume will burn at much higher altitudes than a turbulent one since molecular mixing alone is much less effective than turbulence at cooling the plume through mixing with the atmosphere.

The steady state simulations for Case *C*, however, likely overpredict the temperature increase in the plume shear layer due to viscous energy dissipation during transition as altitude is increased. During transition, the shear layer will still be dominated by large scale structures⁹ which will thicken the layer reducing mean shear below what will be realized in a purely laminar case. Thus viscous energy dissipation would be reduced, possibly removing one of the ignition sources mentioned in the previous paragraph. However, small scale turbulent structures which promote increased scalar gradients and enhance molecular mixing are in short supply during transition.⁹ Consequently, as the plume shear layer mixes with the hot core gases it would likely still ignite due to the lack of small scale turbulence to quickly homogenize temperature gradients. The laminarized plume should therefore still burn until an altitude is reached which sufficiently cools the plume core flow by expansion.

Figure 10 presents a plot of the Reynolds number along the plume shear layer for Case A at 35 km. In this figure the Reynolds number is given by,

$$Re_{\delta_1} = \bar{\rho} \Delta U \delta_1 / \bar{\mu} \quad (1)$$

where ΔU is the velocity difference across the layer and the overbar represents the average of the layer edge conditions. The layer thickness δ_1 is the distance between the points $U_1 - 0.1\Delta U$ and $U_2 + 0.1\Delta U$ where U_1 and U_2 are the high and low speed layer edge velocities, respectively. The oscillations seen in this figure downstream of $x/x_{refl} \approx 1.5$ result from compression and expansion wave interactions with the shear layer downstream of the barrel shock reflection point. From the compressible shear layer experiments of Goebel and Dutton,¹⁵ the layer should be transitioned to a fully developed turbulent flow by $Re_{\delta_1} = 1 \times 10^5$. From Figure 10, this value of Re_{δ_1} is reached very close to the nozzle exit plane. However, this transition value of Re_{δ_1} does not account for pressure gradient and curvature effects present in plume flows. Even so, the plume shear layer Reynolds number becomes quite high further downstream and can therefore be expected to be fully turbulent. Based on Figure 10 and the arguments of the previous paragraph, the relaminarization/mixing transition mechanism to produce afterburning shutdown of fuel rich exhaust plumes is implausible.

Another mechanism discussed in Section 1 which may be responsible for afterburning shutdown is a Damköhler number effect. The Damköhler number, Da , is the ratio of representative mixing and chemical time scales (i.e., $Da = \tau_{mix}/\tau_{chem}$) and characterizes the competition between plume cooling due to turbulent mixing and plume heating due to chemical heat release and combustion. Afterburning in exhaust plumes will not be sustained when turbulent mixing can cool the plume at a rate higher than chemical processes can produce

heat and a radical pool sufficient to initiate burning. A characteristic mixing time, τ_{mix} , may be calculated as the time of flight of a particle traveling from the nozzle to the downstream location where the shear layer reaches the axis of symmetry. A characteristic chemical time, τ_{chem} , may be calculated in a similar manner as used by Mungal and Frier, ¹⁶ given the mean nozzle species and ambient conditions. As the altitude is increased, τ_{chem} will increase due to falling reactant concentrations. The mixing time will also increase due to lowering ambient pressure and Reynolds number.

Figure 11 presents a plot of Da as a function of altitude for Case A. The falling value of Da seen in this plot indicates that τ_{chem} increases more quickly with altitude than τ_{mix} . This falling Damköhler number explains why afterburning shuts down in the present simulations. It also explains the increased standoff distance of vigorous afterburning seen for the cases in Figure 8. For Case D with enhanced mixing, Da will be lower than for Case A resulting in the increased drop off rate of the total intensity as seen in Figure 9. This Damköhler number mechanism for afterburning shutdown will generally produce gradual drop off rates of plume radiation as observed in present simulations. However, the drop off rate produced by this mechanism will be dependent on the ignition characteristics of the fuel species within the plume.

It should be noted that this Damköhler number mechanism not only produces the afterburning shutdown observed in the present simulations but it is also the *only* shutdown mechanism modeled within GASP and most commercially available codes. This results from the assumption that the effect of turbulent fluctuations on the mean reaction rate are negligible as discussed in Section 2. Consequently, the flame extinction shutdown mechanism introduced in Section 1 cannot be evaluated directly using GASP because this phenomena

is a result of the interaction of turbulence and chemistry at small spatial scales.

To evaluate the flame extinction mechanism for afterburning shutdown, an overlay procedure was developed based on an elementary flame extinction model¹⁷ applicable to high speed flows. This model was applied by Sloan and Sturgess¹⁷ in the context of a low speed coannular step combustor and is based on the Eddy Dissipation Concept (EDC) turbulent-chemistry interaction model of Magnussen and Hjertager.¹⁸ The EDC is a distributed reaction model (or thick flame model) and assumes the fine scale turbulent structures, within which combustion occurs, to be homogeneously mixed. Combustion within these structures is then represented by a constant pressure, adiabatic Perfectly Stirred Reactor (PSR) model.¹⁹ The residence time, τ , of this "reactor" is specified as the local hydrodynamics time scale of the micro-scale structures, which is the inverse of the small scale strain rate, s . This strain rate is estimated from the turbulence model as,

$$s = \frac{1}{\tau} = C_s \left(\frac{\varepsilon}{\nu} \right)^{1/2} \quad (2)$$

where ε , ν and C_s , are the turbulent kinetic energy dissipation rate, the laminar mixture viscosity and a calibration coefficient, respectively. Given this strain rate or time scale, the local fluid mixture is allowed to react in the PSR. If the local strain rate is too high (or the time scale too small), no combustion will occur and the mixture is extinguished. For lower strain rates, the mixture will ignite and combustion products will be formed. This model is in effect a Damköhler number based mechanism similar to what is currently employed within GASP by assumption (as discussed earlier). However, Da for this model is based on the micro-scale time as opposed to GASP which implicitly uses a large scale mixing time.

This simplistic extinction model provides a binary on/off switch for the chemical source term in the species conservation equations. Given the local turbulent strain rate and fluid mixture, the model uses the PSR calculation to determine if burning is extinguished. If extinguished, the mean reaction rate in the species conservation equation should be set to zero, otherwise chemical reactions are allowed.

Other more comprehensive extinction models do exist such as the thin flame model of Peters and Williams.²⁰ However, models of this type are inapplicable in their current form to the type of high speed flows encountered here. These models represent the local thermochemical state by a collection or "library" of laminar opposed flow diffusion flames given an assumed joint probability distribution function of mixture fraction and flame stretch parameter,²¹ coupled with an extinction criteria. These models require *apriori* knowledge of local flow conditions to generate the library of opposed flow flames. However, local conditions are unknown in the present context because there are large variations in pressure and temperature in both the fuel and oxidizer streams due to high compressibility and viscous energy dissipation within the plume shear layer. Also, nonuniformities in the nozzle exhaust stream preclude the definition of a single mixture fraction variable. As a result, the simplistic EDC based extinction model appears to be one of the few, if not the only, such models applicable to the present flow regime.

To apply the EDC based extinction model to high speed plume flows would require integrating the PSR calculations within the main code. However, this can be prohibitive due to the increased computational expense of the PSR calculations as the extinction limit is approached as noted by Sloan and Sturgess.¹⁷ Therefore, since the purpose of this investigation was to evaluate the validity of the flame extinction mechanism to produce afterburning

shutdown and not to make quantitative predictions, the EDC based extinction model was implemented in an uncoupled overlay calculation. A code was written to make an uncoupled calculation of the binary switch value for the extinction model given a converged flowfield solution. For this uncoupled analysis to be meaningful, the calculation must be made on a nonreacting flowfield because extinguished regions of the flow with high local strain produce the nonreacting solution.

Figure 12 presents a contour plot of the binary switch for Case *B* at altitudes of 25, 30 and 35 *km*. The streamwise axis for each altitude has been scaled by x_{refl} . For this calculation, $C_s = 0.03$ as will be discussed later. The black regions of the plot for each altitude represent the "on" value for the chemistry while the white areas represent the "off" value. From Figure 12, the extinction model predicts the 25 *km* case to have essentially no extinct locations in the plume shear layer. For 30 *km*, the model predicts that much of the plume is extinguished with burning allowed in the plume farfield. At 35 *km*, the plume flame is extinguished. This is an interesting result because plots of the local strain rate show that it is falling with increasing altitude due to falling turbulence levels. This may be seen in Figure 13 which is a plot of the local strain rate across the plume at a streamwise distance of $x/x_{refl} = 2$. The values of s in the plume shear layer is seen to drop dramatically with increasing altitude. This fact would at first glance appear to rule out the strain rate extinction mechanism for afterburning shutdown. However, the reaction rates (or small scale Damköhler number) are decreasing with altitude faster than the local strain rate so that the extinction limit is reached producing the characteristics seen in Figure 12.

Values found in the literature for the coefficient C_s in Equation (2) range from 0.05758 – 2.43, with a value of 2.43 being used by Sloan and Sturgess.¹⁷ These values are generally

determined by matching model results for flame standoff distance with experimental data for low Mach number turbulent jet flames. Consequently, these calibration values likely do not apply to high Mach number compressible flames encountered in exhaust plumes. Calculations using $C_s = 2.43$, following Sloan and Sturgess,¹⁷ predicted extinction for the entire plume at all simulated altitudes. With $C_s = 0.05758$, the simulations at 30 and 35 km were completely extinguished, while at 25 km the plume was mostly extinguished. The value of $C_s = 0.03$ was chosen because it was the closest value to the range found in the literature which produced a fully afterburning plume at 25 km, in qualitative agreement with observations of real amine boosters similar to the generic configuration investigated here. To fully implement this model with GASP, however, would require a rigorous calibration study to determine the value of C_s applicable to high speed plume flows. However, the present value of $C_s = 0.03$ was reasonable for the present purpose of demonstrating the viability of the strain rate extinction mechanism for afterburning shutdown.

To estimate the effect of the extinction model on the flow results, Case *B* was rerun with the chemistry turned on at axial locations corresponding to "on" values plotted in Figure 12. Figure 14 compares the temperature field for the extinction model case with Case *A* results at 30 km. The extinction model clearly has a major impact on the combustion characteristic within the plume. The model shows a large delay distance before a rapid rise in temperature occurs as turbulent strain rates drop below the extinction limit. Conversely, Case *A* results show a somewhat gradual rise in temperature along the plume as afterburning is initiated.

The modified temperature distribution for the strain rate extinction model seen in Figure 14 has a major impact on the spatial radiance distribution as seen in Figure 15. Also included in the figure are the results for Case *A* at 30 km. This figure shows that the delay in ignition

resulting from the extinction model produces a long delay in high levels of radiation intensity, significantly changing the character of the spatial emission. This type of behavior has been observed for some missile systems. Integrated station radiation was also strongly affected by the extinction model as seen in Figure 16. The extinction model causes the station radiation to exhibit a sharp rise once plume ignition occurs and significantly reduces the peak value that is realized. Total intensity plots (not shown) also show the model to dramatically increase the drop off rate of the afterburning shutdown event. These are significant findings because the dramatic impact of the strain rate extinction model seen in the previous figures will have a significant impact on the total heat transfer to the booster base region and the development of missile defense systems. These results also demonstrate the viability of this previously unrecognized phenomena occurring in rocket exhaust plumes.

Finally, to demonstrate the adequacy of the computational grid resolution, Figures 17 and 18 present plots of the temperature and CO_2 mole fraction at two locations in the plume for Case A at 25, 30 and 35 km. Shown in the figures are results for the plume solutions on the original (fine) grid and a coarse grid with half as many point in each coordinate direction. As seen in these figures, only small differences are evident in the solutions indicating that the original grids adequately resolved the flowfields.

5 Conclusions

A computational study was undertaken to assess the validity of physical mechanisms believed to contribute to afterburning cessation in fuel rich missile exhaust plumes. Several mechanisms were investigated: 1) a relaminarization phenomenon, 2) a Damköhler number effect and 3) a classical flame extinction mechanism. Analysis of the simulation results lead

to the following conclusions:

1. The relaminarization mechanism for afterburning shutdown was found to be implausible for the following reasons. First, hot plume core gases and high temperatures in the plume shear layer, due to viscous energy dissipation, provide an ignition source for unburned fuel to high altitudes. As a result, a purely laminar plume will burn at much higher altitudes than a turbulent one. Second, calculated plume shear layer Reynolds numbers for the high altitude case show the layer to still be well above the transition Reynolds number after afterburning shutdown has occurred.
2. The Damköhler number mechanism for afterburning shutdown was found to be plausible and indeed the only shutdown mechanism modeled within most commercially available codes. This results from the assumptions used to model the mean reaction rate in the species conservation equations. This mechanism was found to be responsible for the gradual drop off rates of plume radiation produced by the GASP code. The drop off rate produced by this mechanism, however, will be highly dependent on the ignition characteristics of the fuel species within the plume. However, it seems unlikely that chemistry effects alone could produce the steep drop off rates which have been observed for many systems.
3. The classical flame extinction mechanism was also found to be a plausible afterburning shutdown mechanism. Overlay calculations employing this mechanism produced dramatic changes in the spatial, station and total radiation emissions. This mechanism was also found to significantly enhance shutdown and offers a likely explanation for the rapid shutdown behavior observed for many systems. This is a significant finding because strain induced flame extinction is a previously unrecognized phenomena occurring

in rocket exhaust plumes during afterburning shutdown.

ACKNOWLEDGMENT

This work was supported by the Air Force Research Laboratory, Edwards AFB, CA and the Ballistic Missile Defense Organization under PL SETA Contract No. F04611-96-C-0001. Support for some of the computations was provided by the DOD High Performance Computing Centers at the Tank-Automotive Research, Development & Engineering Center, Warren, MI and is gratefully acknowledged.

6 REFERENCES

- [1] Reijasse, P. and Détery, J., "Investigation of the Flow Past the ARIANE 5 Launcher Afterbody," *Journal of Spacecraft and Rockets*, Vol. 31, No. 2, 1994 pp. 208-214.
- [2] Kramer, O.G., "Evaluation of Thermal Radiation from the TITAN III Solid Rocket Motor Exhaust Plumes," AIAA Paper 70-842, Jun. 1970.
- [3] Pearce, B.E. and Varma, A.K., "Radiation-Turbulence Interaction in a Tactical Missile Exhaust Plume," AIAA Paper 81-1110, Jun. 1981.
- [4] Dash, S.M., Pearce, B.E., Pergament, H.S. and Fishburne, E.S., "Prediction of Rocket Plume Flowfields for Infrared Signature Studies," *Journal of Spacecraft and Rockets*, Vol. 17, No. 3, 1980, pp. 190-199.
- [5] Norris, J.W. and Edwards, J.R., "Large-Eddy Simulation of High-speed, Turbulent Diffusion Flames with Detailed Chemistry," AIAA Paper 97-0370, Jan. 1997.
- [6] Schadow, K.C., Gutmark, E., Parr, T.P., Parr, D.M. and Wilsion, K.J., "Enhancement of Fine-Scale Turbulence for Improving Fuel-Rich Plume Combustion," *Journal of Propulsion and Power*, Vol. 6, No. 4, 1990, pp. 357-363.

- [7] Lee, S.R. and Netzer, D.W., "The Effects of Particulates on Supersonic Shear Layers and Afterburning in Fuel-Rich Plumes," *Proceedings of the JANNAF 22nd Exhaust Plume Technology Meeting*, 1995.
- [8] Dash, S.M., "Rocket Motor Plume Flowfields: Phenomenology and Simulation," *AGARD Lecture Series 188*, Rocket Motor Plume Technology, AGARD-LS-188, 1993.
- [9] Breidenthal, R., "Structure in Turbulent Mixing Layers and Wakes Using a Chemical Reaction," *Journal of Fluid Mech.*, Vol. 109, 1981, pp. 1-24.
- [10] Walters, W.R., Cinnella, D.C. and Halt, S.D., "Characteristic-Based Algorithms for Flows in Thermochemical Non-Equilibrium," *AIAA Journal*, Vol. 30, No. 5, 1989, pp. 1304-1313.
- [11] Ludwig, C.B., Malkmus, W., Walker, J., Slack, M. and Reed, R., "The Standard Infrared Radiation Model," *AIAA Paper 81-1051*, Jun. 1981.
- [12] Nelson, H. F., "Evaluation of Rocket Plume Signature Uncertainties," *Journal of Spacecraft and Rockets*, Vol. 24, No. 6, 1987, pp. 546-551.
- [13] Chien, K.-Y., "Predictions of Channel and Boundary-Layer Flows With a Low-Reynolds-Number Turbulence Model," *AIAA Journal*, Vol. 20, No. 1, 1982, pp. 33-38.
- [14] Nickerson, G.R., Coats, D.E., Dang, A.L., Dunn, S.S. and Kehtarnavaz, H. "Two-Dimensional Kinetics (TDK) Nozzle Performance Computer Program," Volume I, II and III, Contract No. NAS8-36863, 1989.
- [15] Goebel, S.G. and Dutton, J.C., "Experimental Study of Compressible Turbulent Mixing Layers," *AIAA Journal*, Vol. 29, No. 4, 1991, pp. 538-546.
- [16] Mungal, M.G. and Frieler, C.E., "Effect of Damköhler Number in a Turbulent Shear Layer," *Combustion and Flame*, Vol. 17, 1988, pp. 23-34.
- [17] Sloan, D.G. and Sturgess, G.J., Modeling of Local Extinction in Turbulent Flames, in *ASME, International Gas Turbine and Aeroengine Congress and Exposition*, The Hague, Netherlands, June 13-16, 1994, ASME Paper 94-GT-433.

- [18] Magnussen, B.F., and Hjertager, B.H., "On Mathematical Modeling of Turbulent Combustion with Special Emphasis on Soot Formation and Combustion," *Sixteenth Symposium (International) on Combustion*, The Combustion Institute, 1976, pp. 719-729.
- [19] Glarborg, P., Kee, R.J., Grar, J.F. and Miller, J.A., "PSR: A FORTRAN Program for Modeling Well-Stirred Reactors," *Sandia National Laboratories Report SAND86-8209*, 1986.
- [20] Peters, N. and Williams, F.A., "Liftoff Characteristics of Turbulent Jet Diffusion Flames," *AIAA Journal*, Vol. 21, No. 3, 1983, pp. 423-429.
- [21] Sanders, J.P.J. and Lamers, P.G.G., "Modeling and Calculation of Turbulent Lifted Diffusion Flames," *Combustion and Flame*, Vol. 96, 1994, pp. 22-33.

Table 1		
Body-Base-Plume Simulations		
Case	Turbulence	Chemistry
<i>A</i>	yes	finite rate
<i>B</i>	yes	frozen
<i>C</i>	no	finite rate
<i>D</i>	yes, enhanced	finite rate

Figure 1. Schematic of the axisymmetric rocket geometry; $d_2/d_1 = 2$, $d_3/d_1 = 2$, $d_4/d_1 = 50$.

Figure 2. Species mole fraction profiles across the engine exit plane. R is the nozzle exit radius.

Figure 3. Streamwise velocity across the engine exit plane. R is the nozzle exit radius and u_o is the centerline velocity.

Figure 4. Temperature profile across the engine exit plane.

Figure 5. Temperature contours for Case *A* at 25 km, (a) farfield view, (b) nearfield view. The downstream direction is to the right.

Figure 6. CO_2 mole fraction contours for Case *A* at 25 km, (a) farfield view, (b) nearfield view. The downstream direction is to the right.

Figure 7. Variation of CO_2 mole fraction across the plume at $x/x_{refl} = 3$ for Case *A* (δ is the transverse distance between the axis and the point where CO_2 mole fraction is equal to 1×10^{-6}).

Figure 8. Predicted normalized spatial radiance distribution as a function of altitude for (a) Case *A*, (b) Case *C* and (c) Case *D*.

Figure 9. Predicted normalized total radiant intensity as a function of altitude for Cases *A*, *B*, *C* and *D*.

Figure 10. Reynolds number along the plume shear layer for Case *A* at 35 km.

Figure 11. Damköhler number variation with altitude for the Case A.

Figure 12. Contour plot of the strain extinction model binary switch for Case B at altitudes of (a) 25, (b) 30 and (c) 35 km. The black region represents "on" values and the white represents "off" values. The x coordinate in each plot has been scaled by x_{refl} .

Figure 13. Predicted small scale strain rate across the plume at $x/x_{refl} = 2$ for Case A.

Figure 14. Comparison of temperature contours at 30 km for Case A (top) and Case B using the strain extinction overlay technique (bottom). The streamwise axial coordinate has been scaled.

Figure 15. Normalized spatial radiance distribution for (a) Case A and (b) Case B using the strain extinction overlay technique.

Figure 16. Normalized station radiation prediction for Case A and Case B using the strain extinction overlay technique.

Figure 17. Plume temperature profiles for the original (fine) and coarse grid solutions of Case A at $x^* = x/x_{refl} = 3$ and 9.

Figure 18. Plume CO_2 mole fraction profiles for the original (fine) and coarse grid solutions of Case A at $x^* = x/x_{refl} = 3$ and 9.

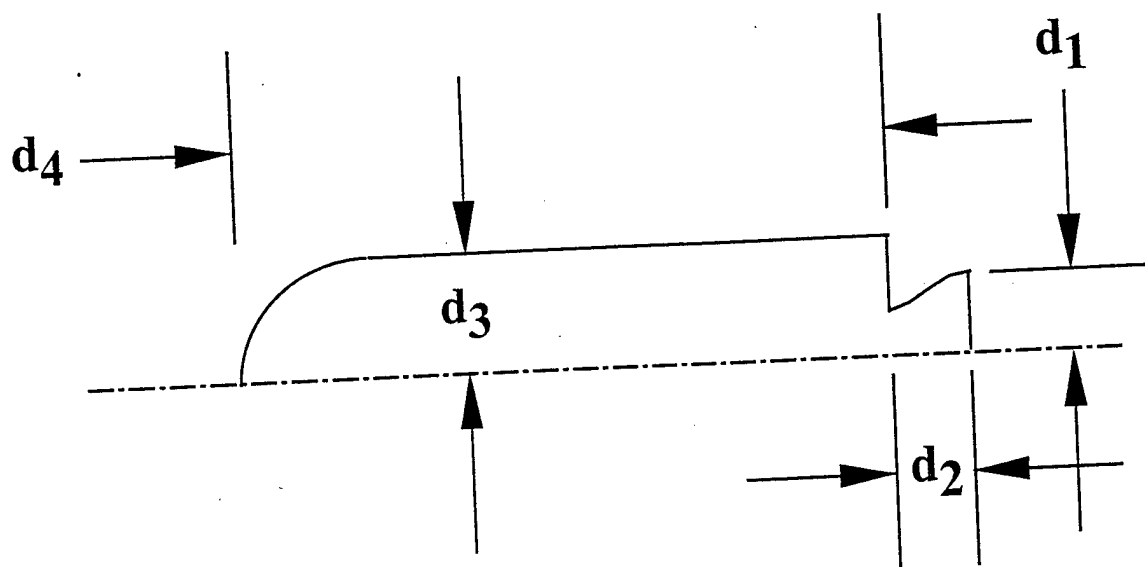


fig. 1
calhoon

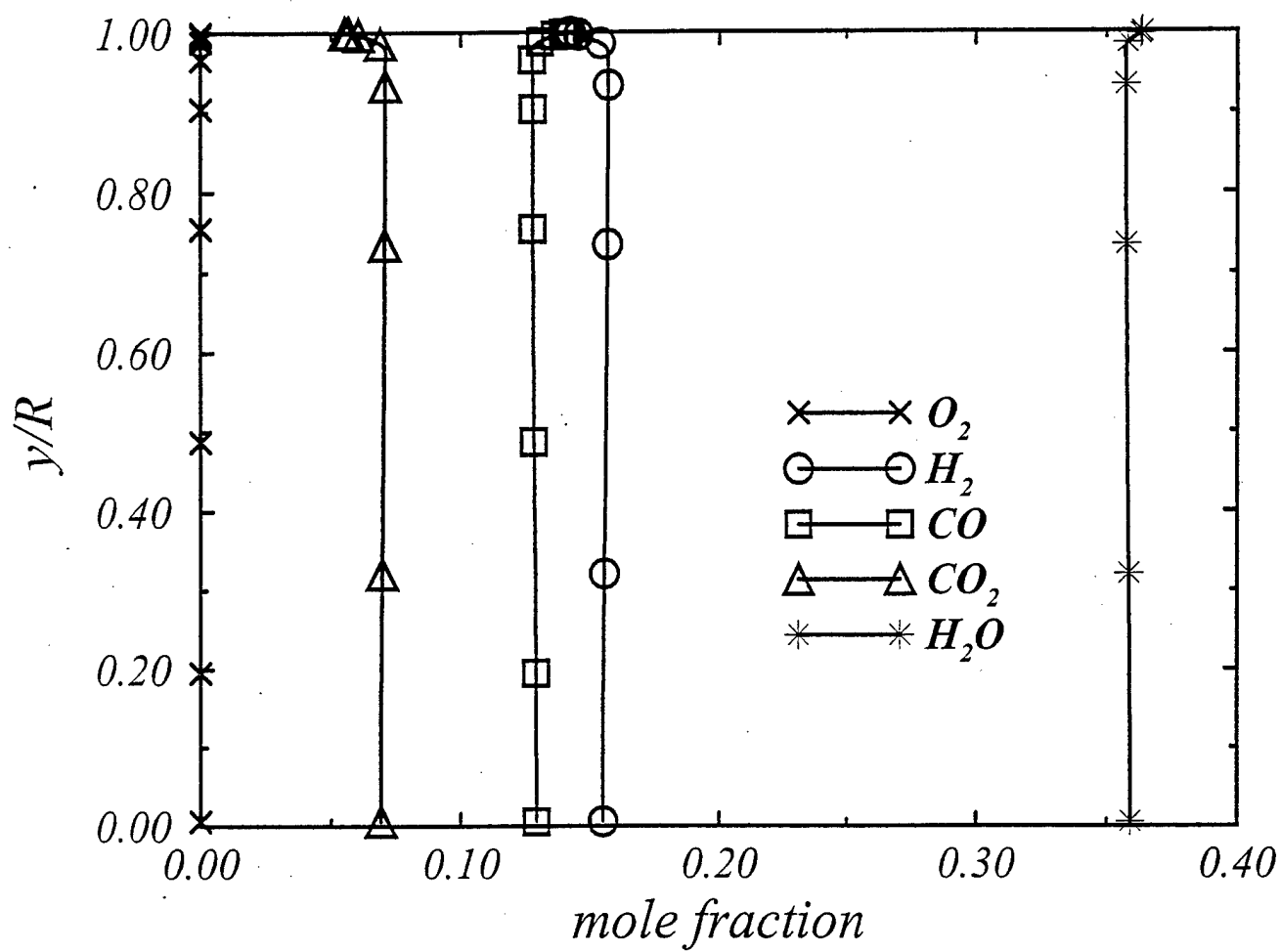


fig. 2
calhoon

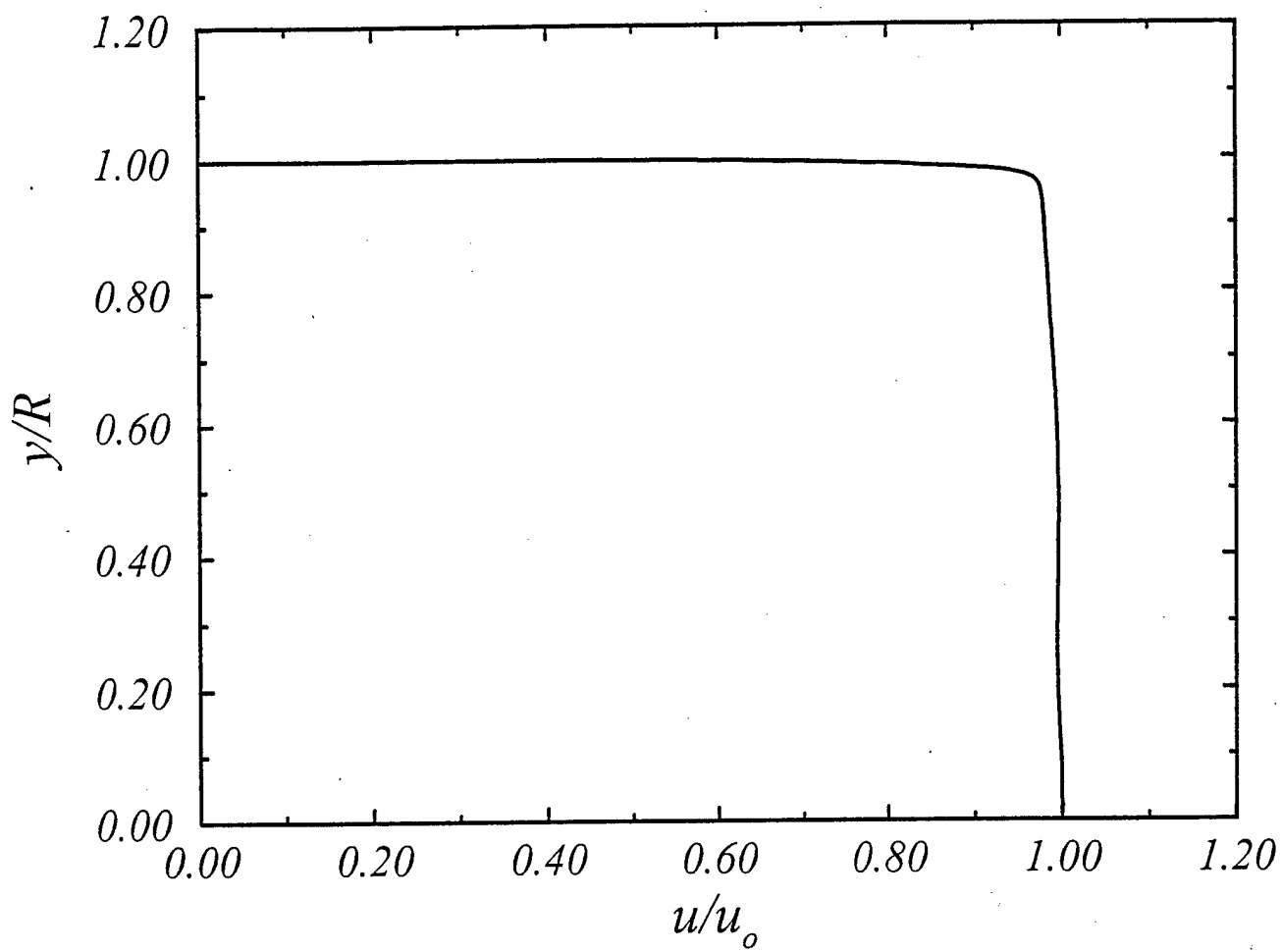


fig. 3
calhoon

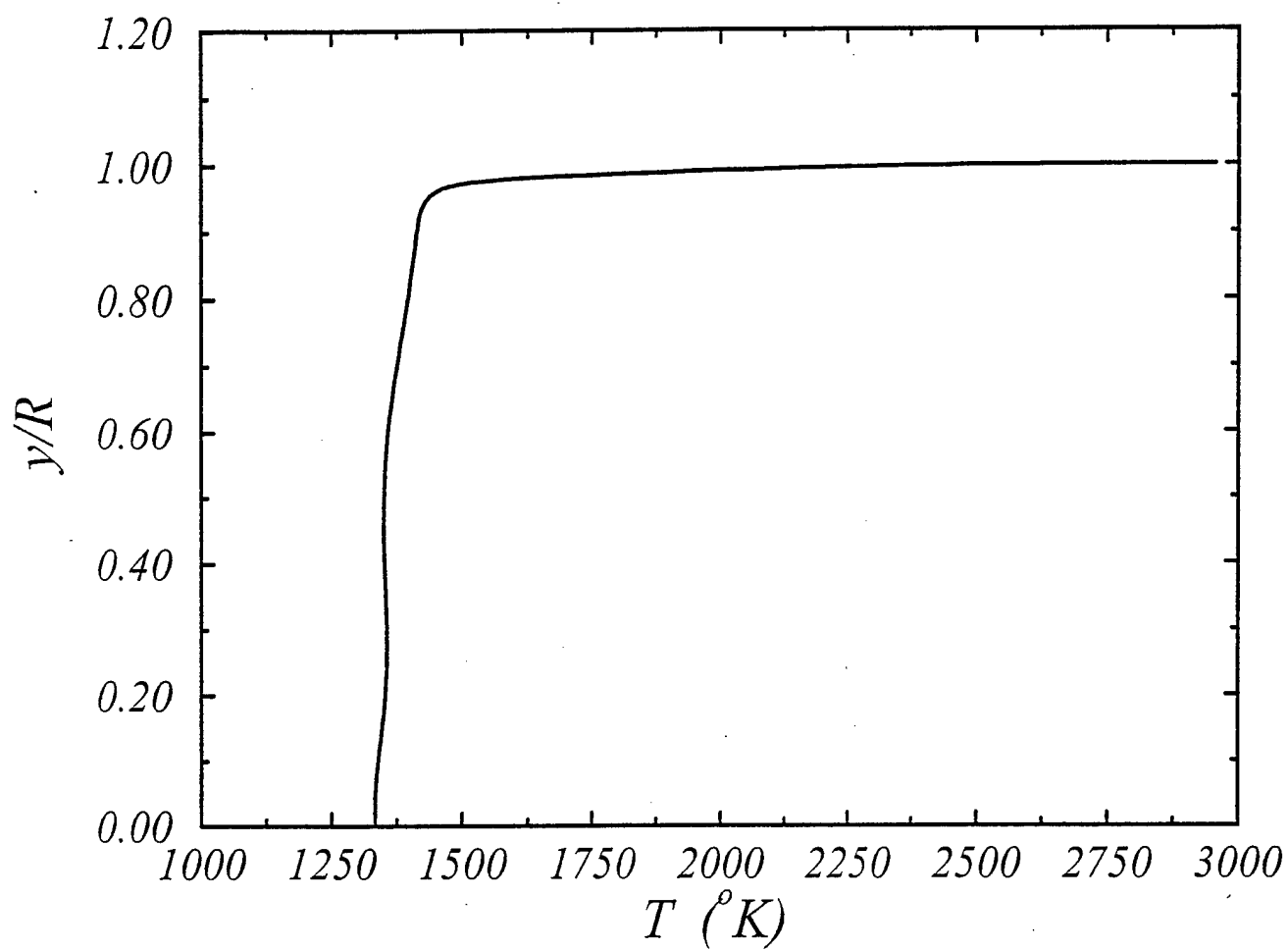


fig. 4
Callhoon

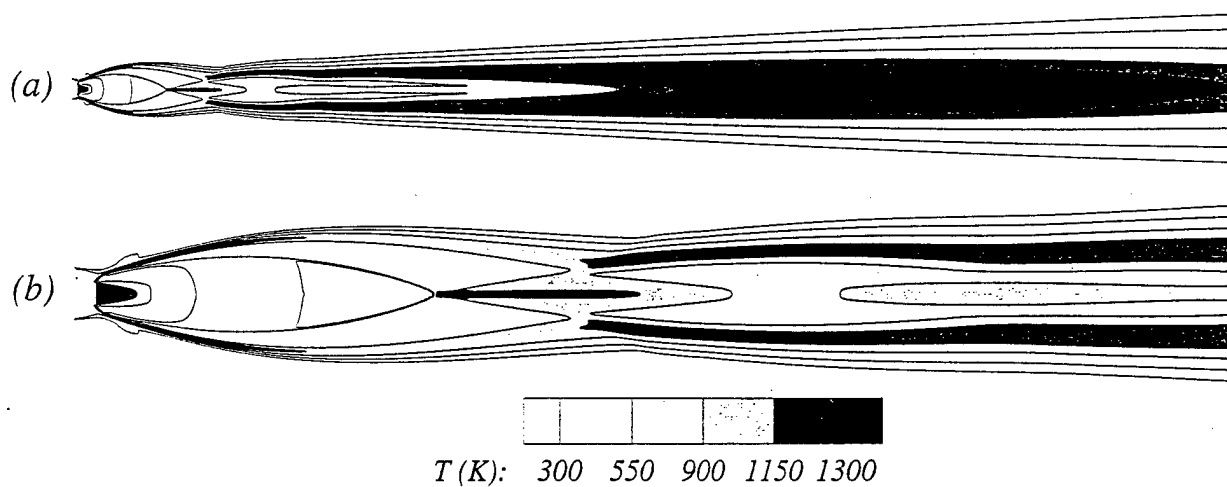


fig. 5
calhoon

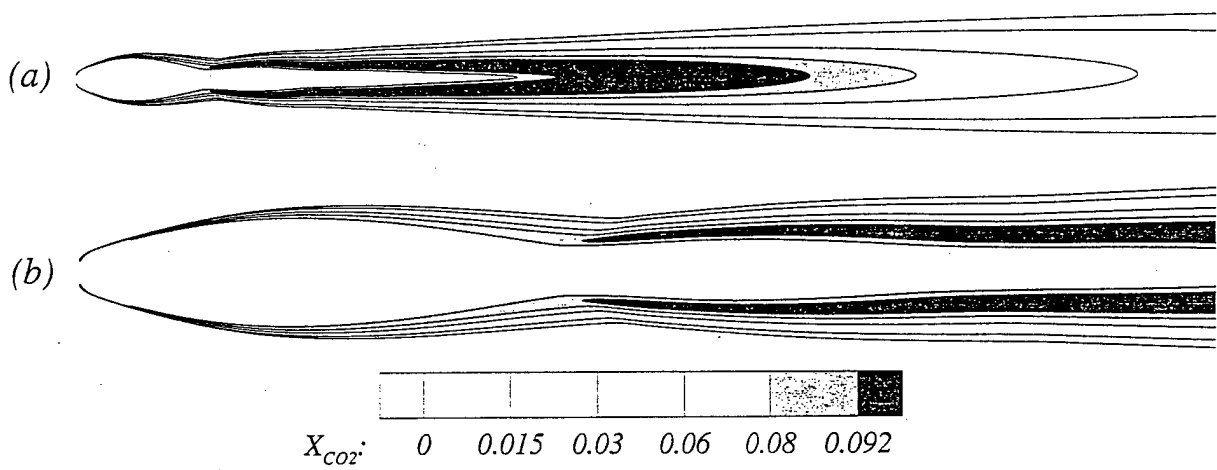


fig. 6
calhoon

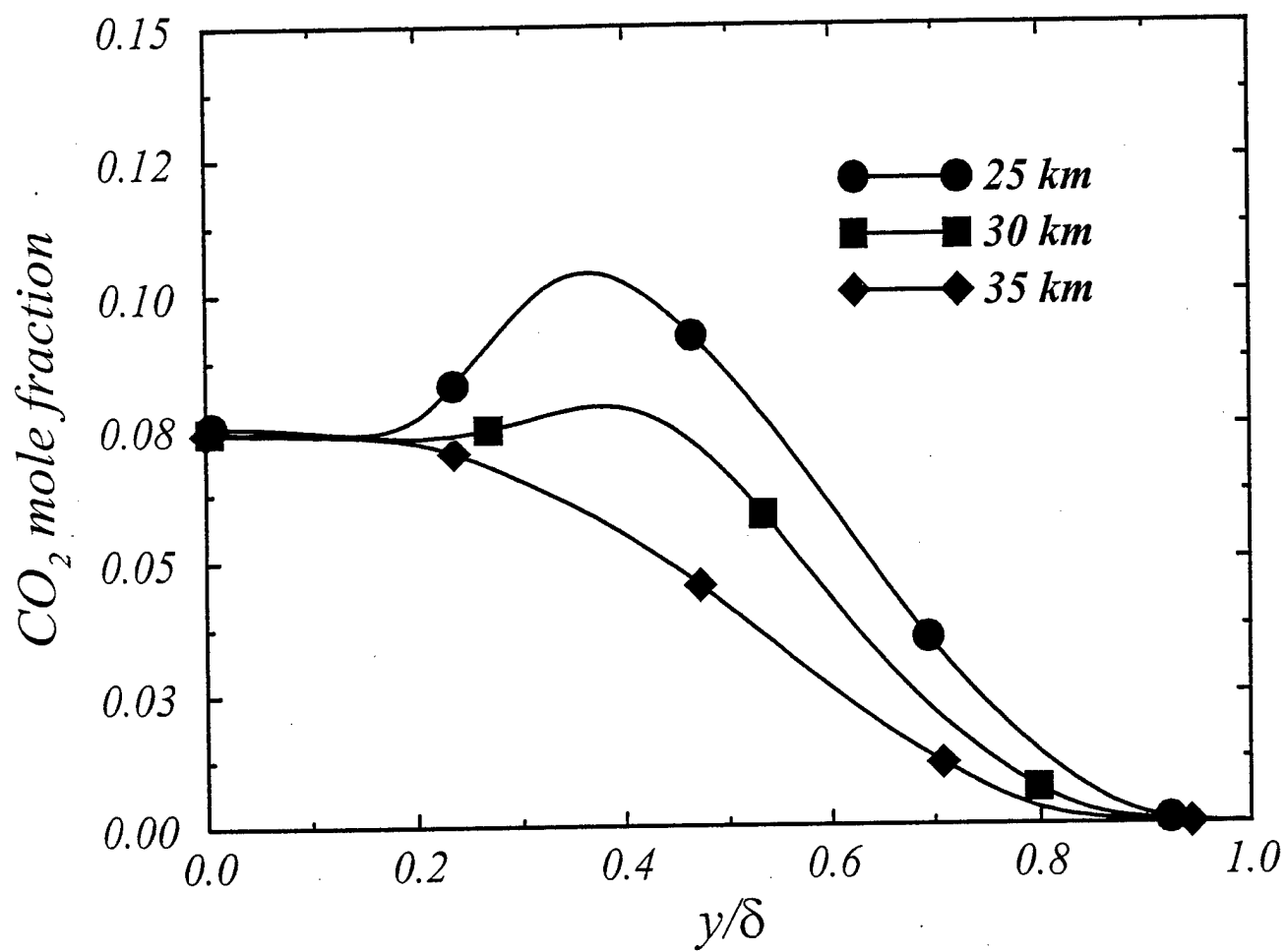


Fig. 7
Callison

35 km

30 km

25 km

(a)

(b)

(c)

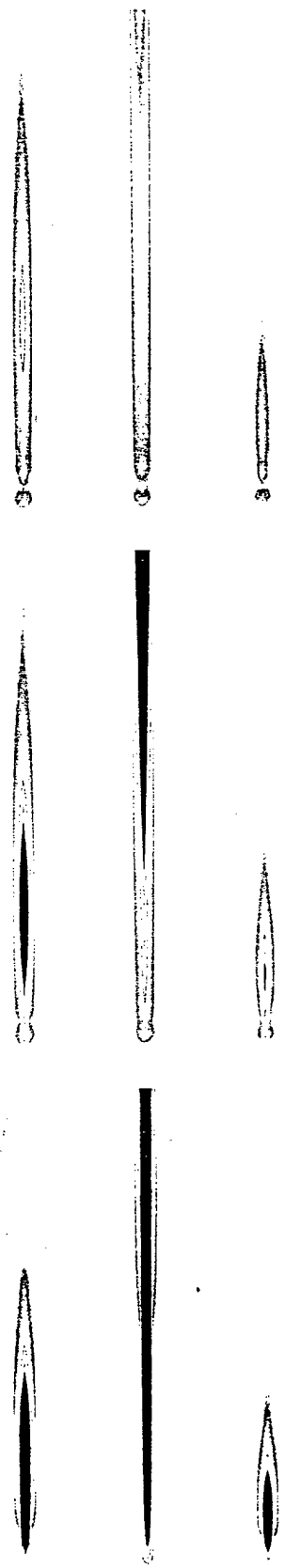


fig. 2
Callison

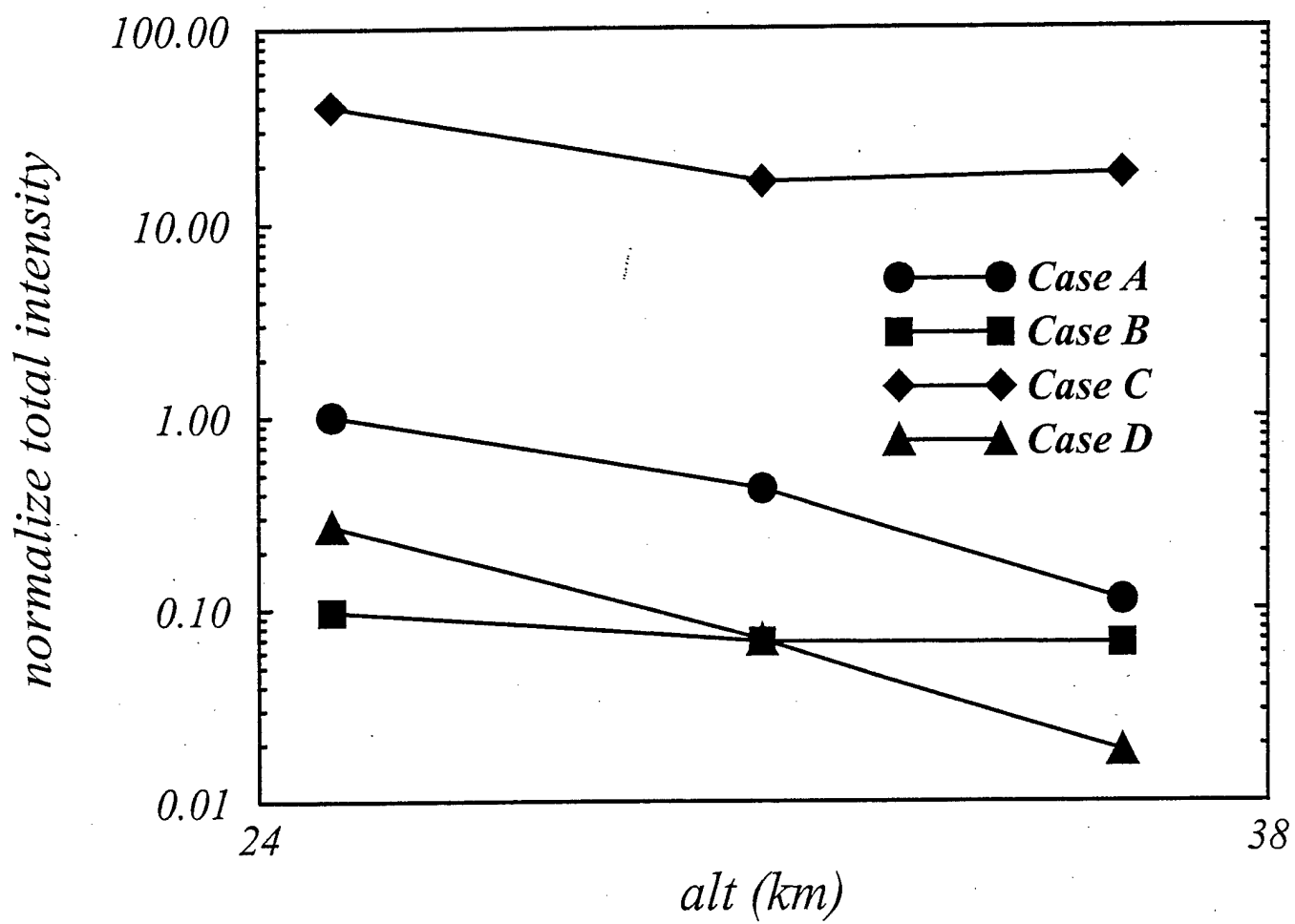


fig. 9

calhoon

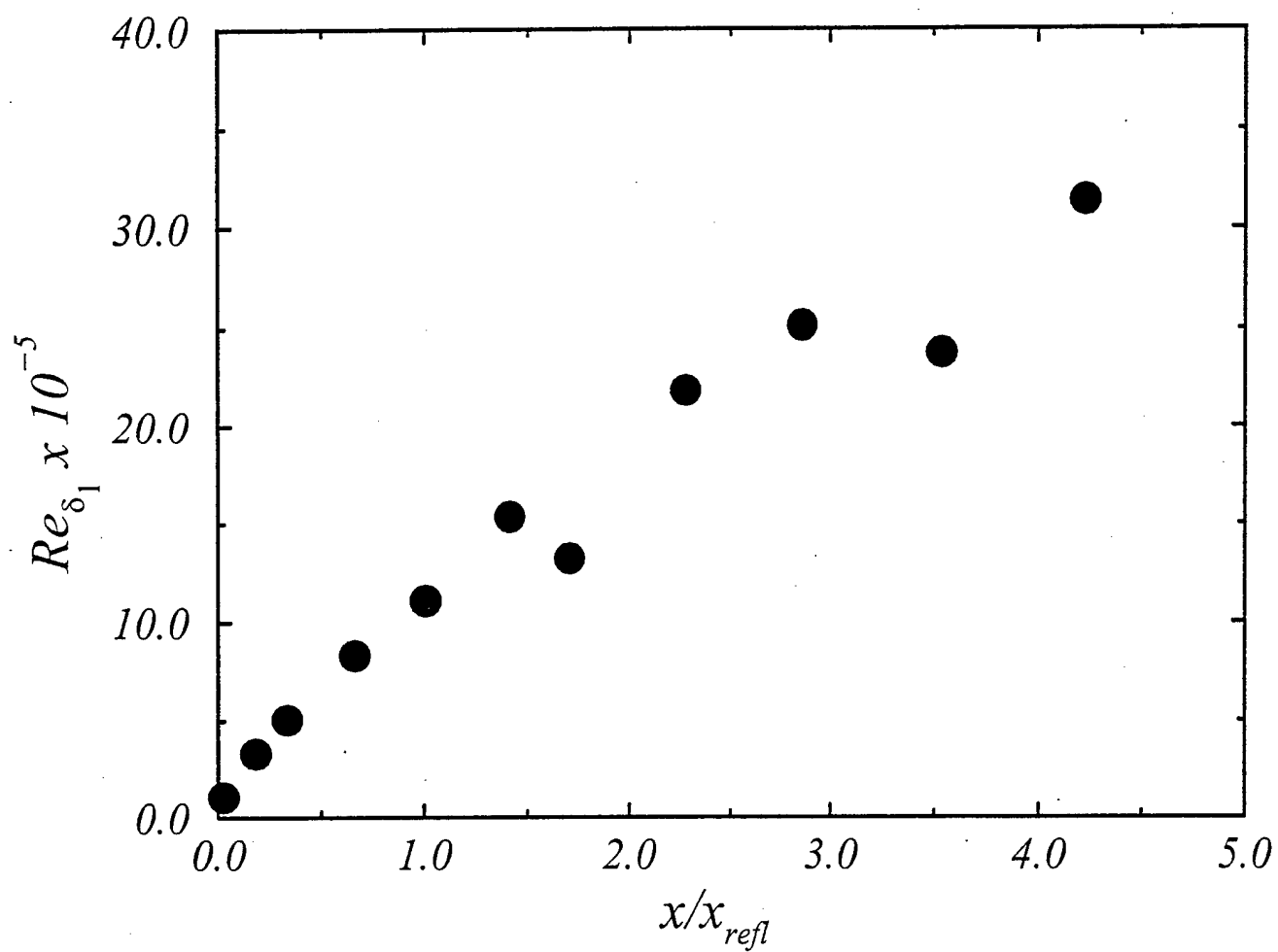


fig. 10

calhoun

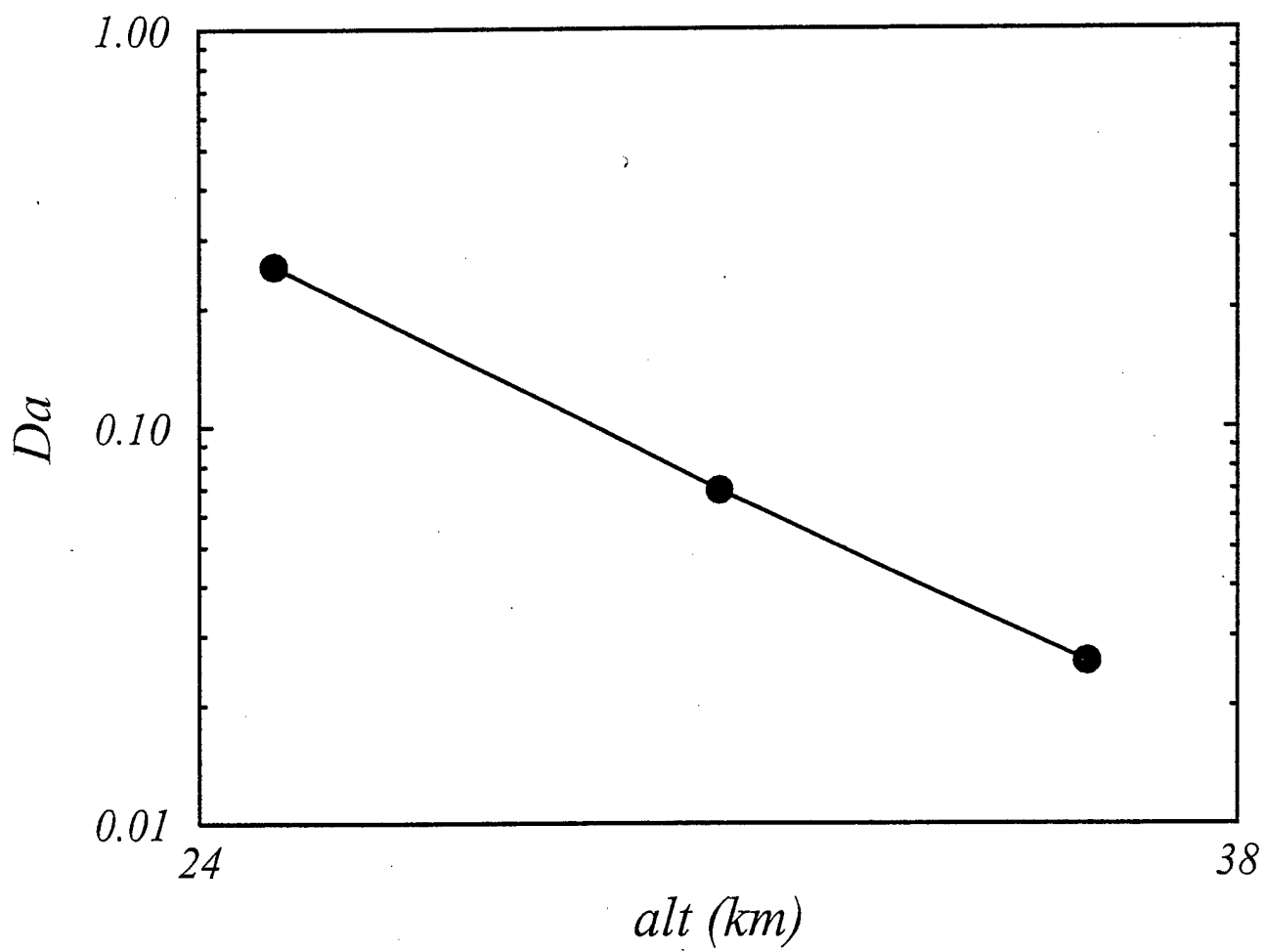


fig. 11
calhoun

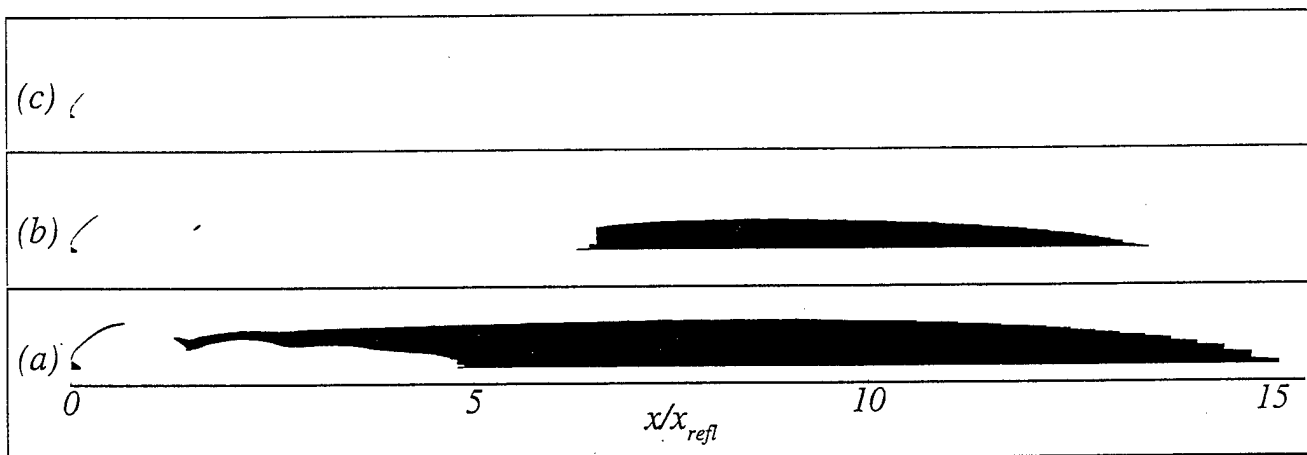


fig. 12

Callwoon

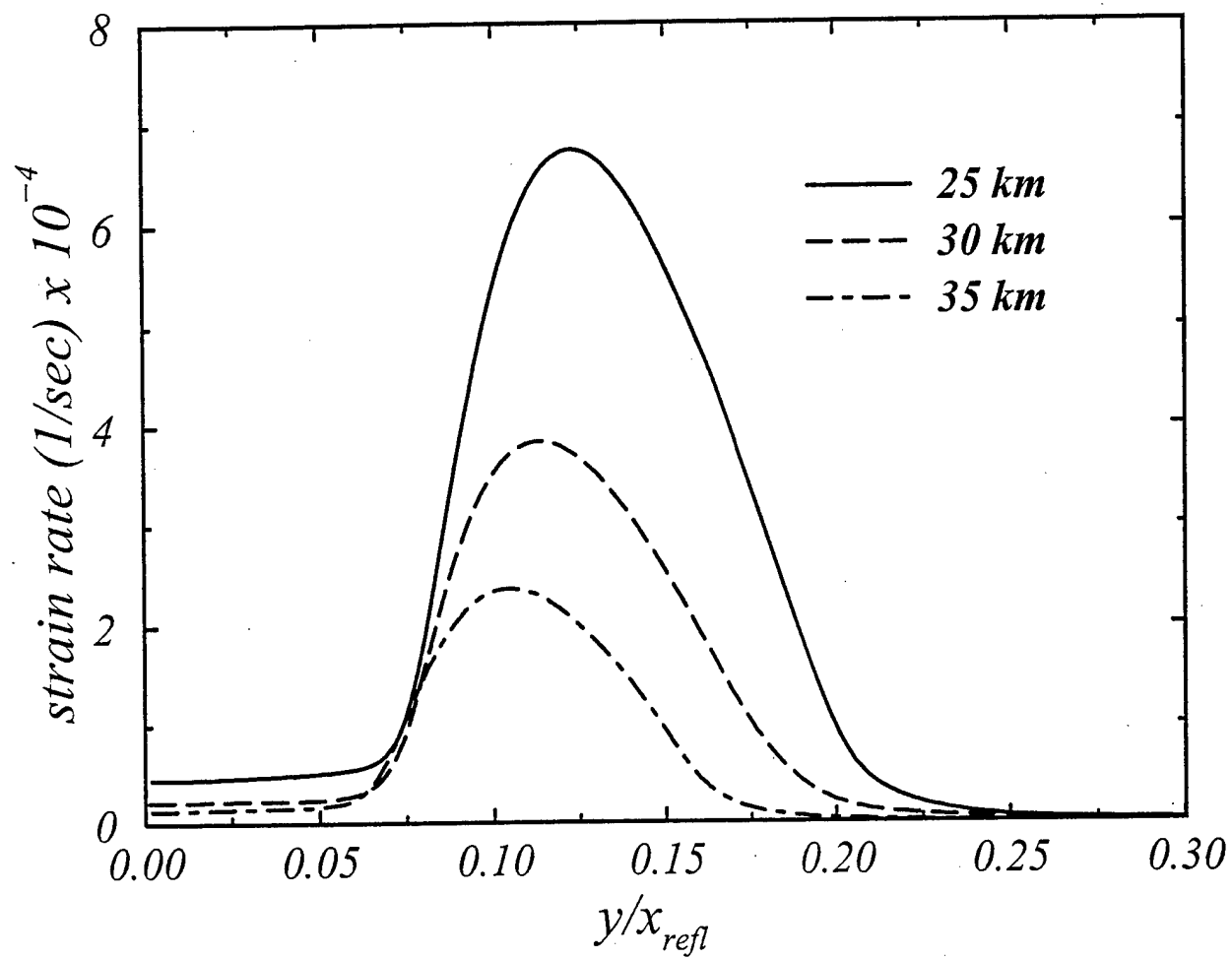


Fig. 13
Callhoon

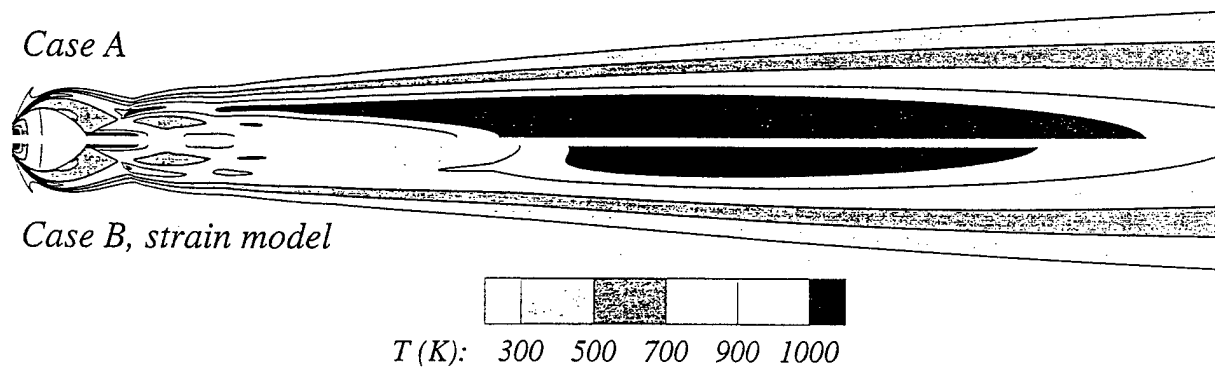


fig. 14
calluon

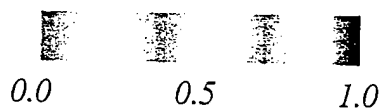
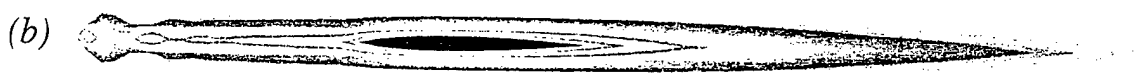
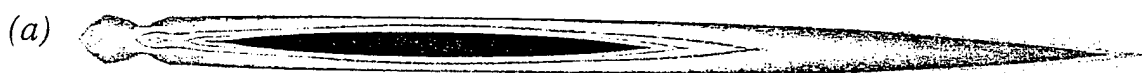


fig. 15
Calluon

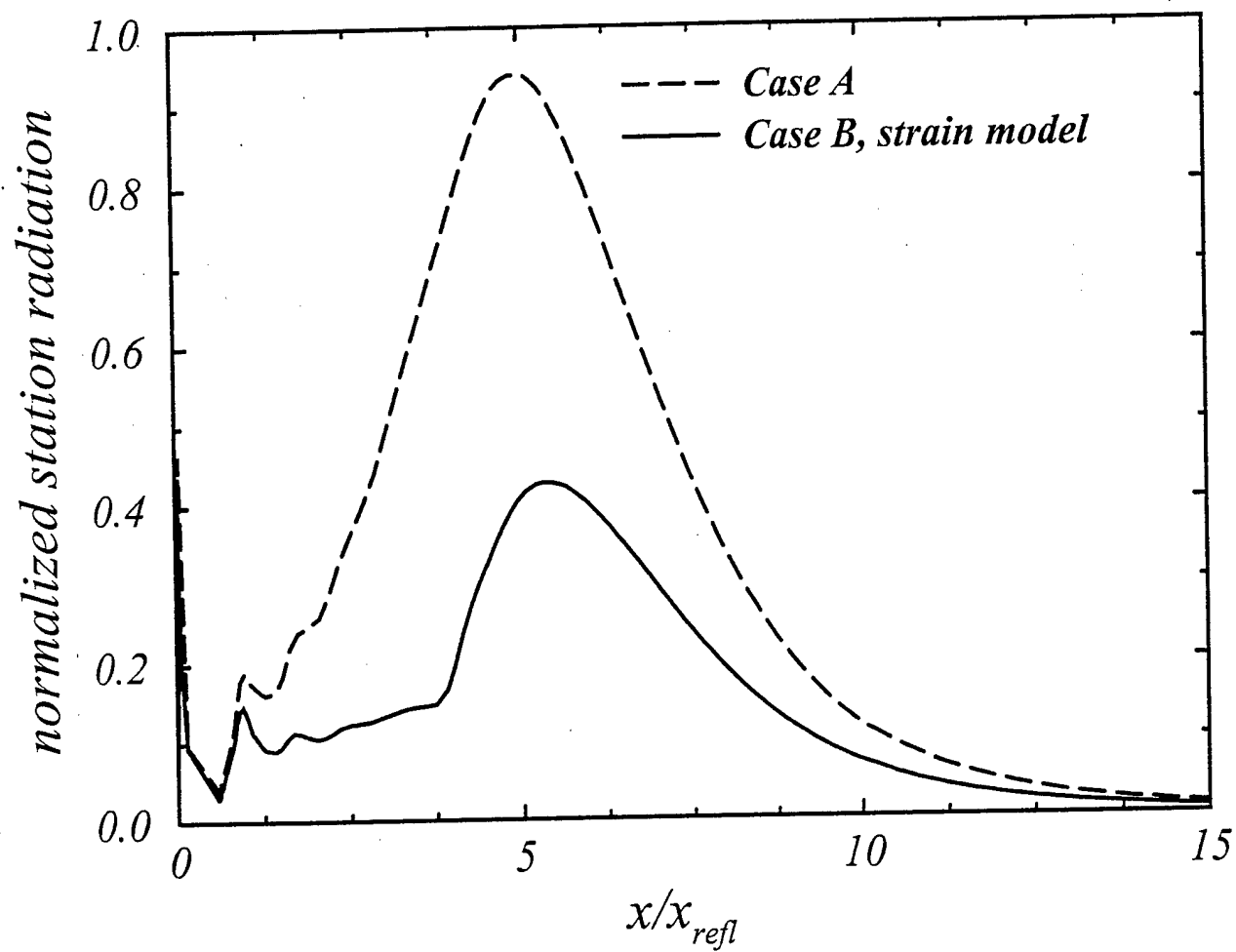


fig. 16
Calhoon

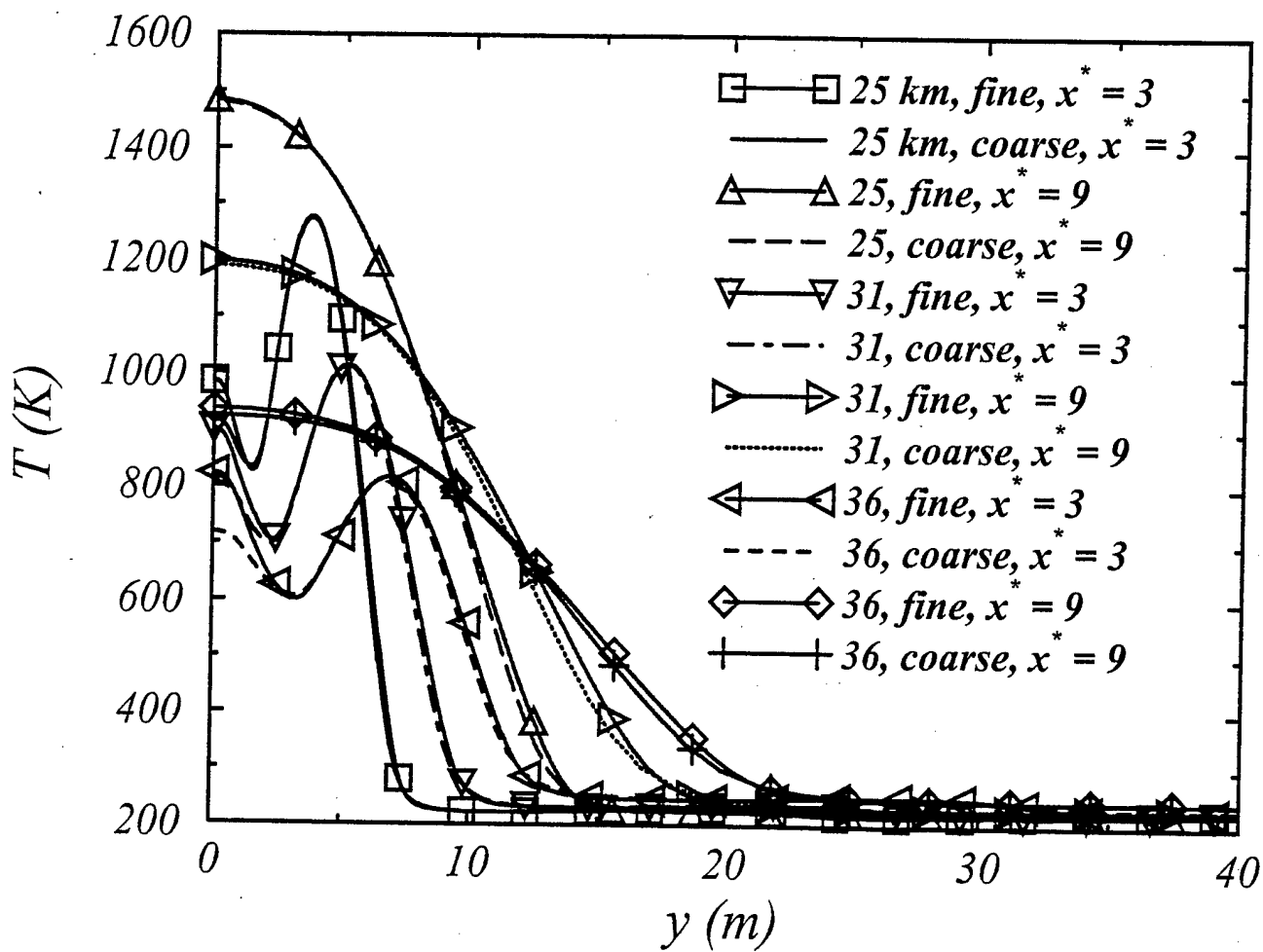


Fig. 17

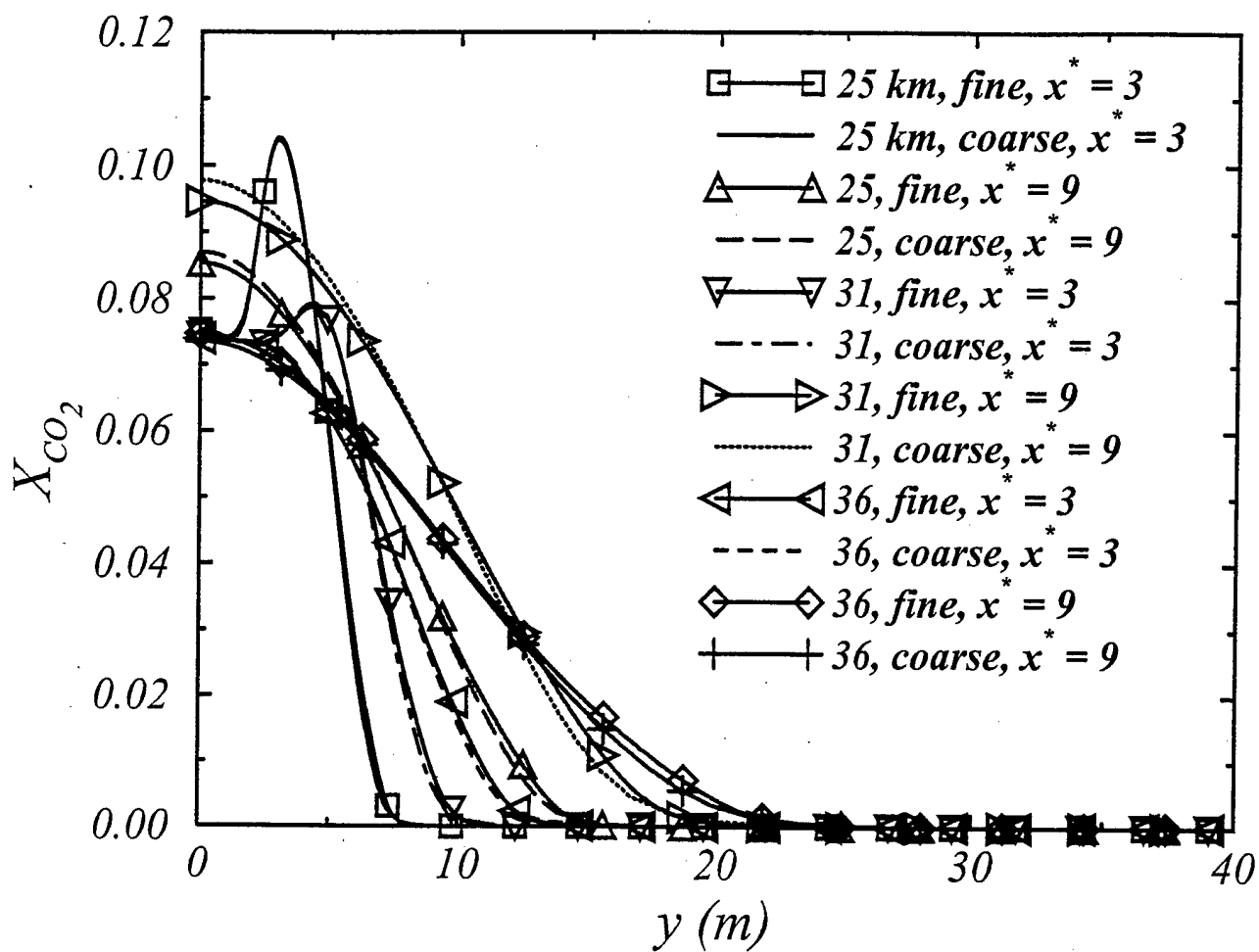


fig. 18